ACS APPLIED MATERIALS & INTERFACES

www.acsami.org
Research Article

Ion Transport at Polymer–Argyrodite Interfaces

Yuxi Chen,[▽] Dongyue Liang,[▽] Elizabeth M. Y. Lee, Sokseiha Muy, Maxime Guillaume, Marc-David Braida, Antoine A. Emery, Nicola Marzari, and Juan J. de Pablo*

Cite This: https://doi.org/10.1021/acsami.4c07440

Read Online

ACCESS | Metrics & More | Article Recommendations | Supporting Information

ABSTRACT: Solid-state electrolytes, particularly polymer/ceramic composite electrolytes, are emerging as promising candidates for lithium-ion batteries due to their high ionic conductivity and mechanical flexibility. The interfaces that arise between the inorganic and organic materials in these composites play a crucial role in ion transport mechanisms. While lithium ions are proposed to diffuse across or parallel to the interface, few studies have directly examined the quantitative impact of these pathways on ion transport and little is known about how they affect the overall conductivity. Here, we present an atomistic study of lithium-ion (Li^+) transport across well-defined polymer–argyrodite interfaces. We present a force field for polymer–argyrodite interfacial systems, and we carry out molecular dynamics and enhanced sampling simulations of several composite systems, including poly(ethylene oxide) (PEO)/Li_6PS_5Cl, hydrogenated nitrile butadiene rubber (HNBR)/Li_6PS_5Cl, and poly(vinylidene fluoride-*co*-hexafluoropropylene) (PVDF-HFP)/Li_6PS_5Cl. For the materials considered here, Li-ion exhibits a preference for the ceramic material, as revealed by free energy differences for Li-ion between the inorganic and the organic polymer phase in excess of 13 k_BT. The relative free energy profiles of Li-ion for different polymeric materials exhibit similar shapes, but their magnitude depends on the strength of interaction between the polymers and Li-ion: the greater the interaction between the polymer and Li-ions, the smaller the free energy difference between the inorganic and organic materials. The influence of the interface is felt over a range of approximately 1.5 nm, after which the behavior of Li-ion in the polymer is comparable to that in the bulk. Near the interface, Li-ion transport primarily occurs parallel to the interfacial plane, and ion mobility is considerably slower near the interface itself, consistent with the reduced segmental mobility of the polymer in the vicinity of the ceramic material. These findings provide insights into ionic complexation and transport mechanisms in composite systems, and will help improve design of improved solid electrolyte systems.

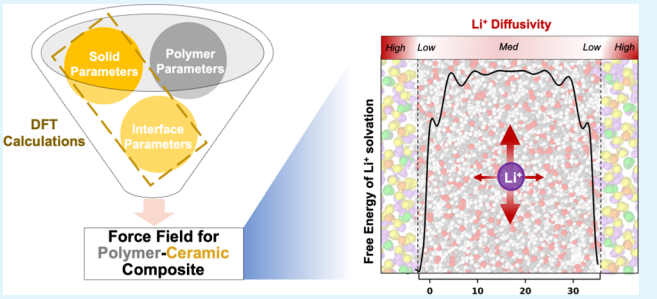

KEYWORDS: *lithium-ion battery, solid-state electrolyte, ion transport, polymer–ceramic interface, force field development, molecular dynamics*

1. INTRODUCTION

Lithium-ion batteries are used extensively in a wide range of applications.[1,2] Unfortunately, a reliance on flammable liquid electrolytes and the formation of lithium dendrites in lithium-ion technologies pose a variety of safety concerns.[3−5] To overcome these challenges and unlock the full potential of safe high-energy-density lithium batteries, solid-state electrolytes have emerged as promising alternatives.[6,7] Two major classes of solid electrolytes, lithium-ion conductive polymers, and lithium-ion conductive ceramics, have been studied extensively; they each have advantages and drawbacks. Ceramic electrolytes offer high conductivity but suffer from brittleness and can have poor interfacial contact between the electrode and the electrolyte.[8−10] Polymer electrolytes, on the other hand, exhibit high electrolyte/electrode interfacial contact and mechanical flexibility, but they suffer from low room-temperature conductivity.[11−15] In recent years, polymer–ceramic composite electrolytes have become an increasingly sought-after solution to harness the benefits of both materials and overcome their limitations. These composite materials offer the potential of improved ionic conductivity, greater mechanical flexibility, and more stable electrode–electrolyte interfacial contacts.[16−18]

Poly(ethylene oxide) (PEO)-based electrolytes exhibit high flexibility, nonflammability, and low cost, but suffer from low ionic conductivity, on the order of 10^{-9} for pure polymers and up to 10^{-4} S/cm for sufficiently high salt contents.[19−22] Among ceramic materials, argyrodite-type compounds such as $LiPS_5X$ (X = Cl, Br, I) have received significant attention as potential electrolytes due to their high ionic conductivity at room

Received: May 6, 2024
Revised: August 8, 2024
Accepted: August 9, 2024

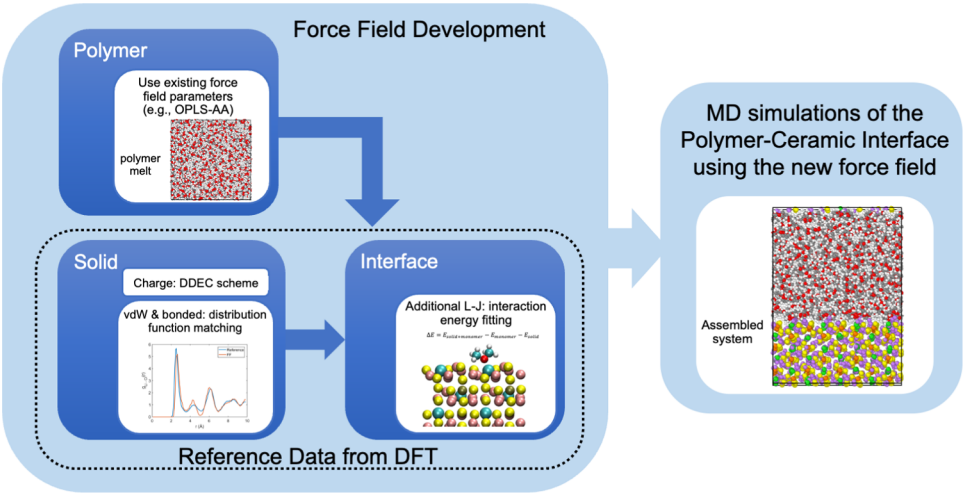

Figure 1. Schematic workflow of force field development and benchmarking presented in this work.

temperature, which can reach approximately 10^{-3} S/cm, high thermal stability, and good processability.[23,24] However, a major drawback associated with these materials is that they tend to decompose upon contact with lithium, rendering them unsuitable for use as standalone electrolytes.[25,26]

Recent advances in polymer/argyrodite electrolytes, particularly PEO/argyrodite systems, have shown potential for battery applications.[26−28] Experimental studies have reported enhanced conductivity and improved adhesion in these composite electrolytes.[26−28] Moreover, the addition of a polymer layer to argyrodites appears to resolve the decomposition issue, showing promise for hybrid electrolytes as materials for next-generation batteries.[26,27] Despite this progress, there are significant gaps in our understanding of the microscopic ion transport mechanisms that govern overall electrolyte conductivity.[29,30] A comprehensive understanding of these mechanisms at the polymer−argyrodite interface is crucial for improving device performance.

Atomistic models and molecular simulations provide ideal tools to interrogate the coupling between molecular-level structure and macroscopic transport in battery electrolytes. Simulations enable access to time and length scales that align well with ion transport phenomena.[29] Indeed, classical molecular dynamics (MD) simulations have been used in recent studies to predict ion transport mechanisms in interfacial systems,[31,32] liquid electrolytes,[5,33] and polymer electrolytes.[29,34−36] Atomistic simulations of composite systems, however, have been limited, owing to the lack of suitable force fields that can accurately describe these heterogeneous interfaces.[37−39] A key challenge lies in the incompatibility between existing force fields, most of which have been parametrized separately for individual inorganic and organic materials. While several force fields for organic materials exist, such as CHARMM,[40,41] Amber[42] and OPLS-AA,[43,44] there are limited force fields for ceramic materials.[45,46] Several studies have sought to develop force fields for organic−inorganic hybrid material, but to date, only a few have been applied to lithium battery materials.[31,32,47,48] Validation of these force fields also remains challenging due to the limited availability of experimental measurements that capture the full molecular-level detail of these heterogeneous interfaces.[48] These existing challenges highlight the need for new developments for atomic-scale simulations of organic−inorganic hybrid energy materials.

In this work, we present a computational workflow for developing force field parameters from *ab initio* calculations, such as density functional theory (DFT), for inorganic−organic interfaces. We show that our force fields describe the polymer/ceramic interfacial interactions, capturing key properties with the accuracy of DFT while providing the computational efficiency of classical MD. Our force fields enable simulations over the length and time scales that are needed to examine lithium transport behavior. The force fields are compatible with a widely used model for polymeric systems, OPLS-AA, thereby providing flexibility in extending this approach to a wide range of polymer electrolytes. Here, we demonstrate the transferability of this computational framework by applying it to three different polymer−argyrodite interfaces. The polymers considered in this study include PEO, hydrogenated nitrile butadiene rubber (HNBR), and poly(vinylidene fluoride-*co*-hexafluoropropylene) (PVDF-HFP). These materials have been considered in composite organic electrolytes and have varying chemical functional groups that interact with Li-ions differently.[49,50] They thus provide a broad platform to investigate how different Li-ion solvation behaviors affect the thermodynamics and kinetics of Li-ion transport in the composite system.

Using our force fields, we then present results from all-atom MD and enhanced sampling simulations of our polymer/Li_6PS_5Cl composite systems. We focus on the structure, thermodynamics, and dynamics of the ceramic/polymer interface and the confined polymeric material. We consider Li-ion solvation and transport in two directions: (1) perpendicular to the interfacial plane, from the ceramic domain to the polymer domain and (2) parallel to the interfacial plane, as a function of the distance to the ceramic phase. More specifically, we calculate the free energy profile of Li-ion in the polymer as a function of distance to the ceramic surface by relying on enhanced sampling simulations. We then examine how the presence of the interface affects the kinetics of Li-ion parallel to the interface at various distances from the interface. Finally, we compare Li-ion stability and kinetics across three polymer systems.

https://doi.org/10.1021/acsami.4c07440
ACS Appl. Mater. Interfaces XXXX, XXX, XXX−XXX

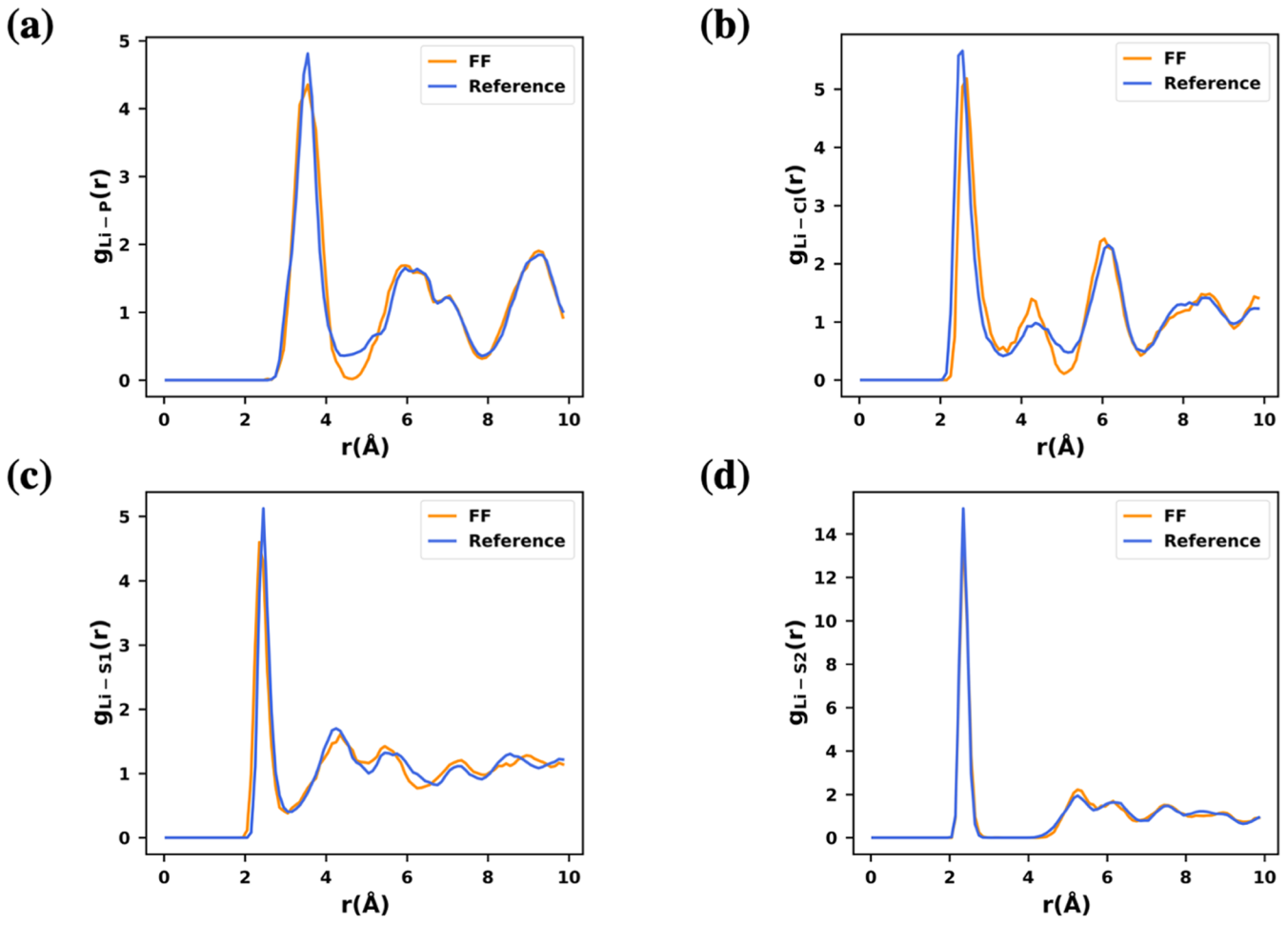

Figure 2. Radial distribution functions (RDF) between Li and other atom types from distribution function matching calculations. The reference refers to the reference distributions obtained from DFT-MD simulations. The rest of the distribution functions are shown in Figure S2. Each figure shows RDF between atom types (a) Li and P (b) Li and Cl, (c) Li and S1 and (d) Li and S2 in the solid, respectively.

2. RESULTS AND DISCUSSION

2.1. Polymer–Argyrodite Force Field Development.

Simulations of ion mobility in polymeric materials typically require calculations ranging from several tens to hundreds of nanoseconds to fully capture the diffusive transport regime.[5,51,52] Simulations of polymer diffusion require even longer time scales. Classical force fields are therefore needed to extensively sample the relevant conformational space and to describe the diffusive behavior of ions. In this work, we use the OPLS-AA model[53] to describe the atomistic interactions between polymer molecules and between polymers and Li-ions. Note that OPLS-AA has already been used and validated for simulations of polymer melts and for Li-ion diffusion in polymers.[5,29] The specific challenge that we address here is that while OPLS-AA force field parameters are available for the polymers of interest to our study, the parameters needed to describe the interatomic interactions within Li_6PS_5Cl and with polymers are not available. To address this gap, we introduce solid and interface force fields based on the OPLS-AA model using results from DFT calculations. Our newly developed polymer–ceramic force fields are compatible with the OPLS-AA model, and they help broaden the range of polymer–ceramic interfacial systems that can be simulated. The proposed workflow is shown in Figure 1.

In the OPLS-AA force field, the total energy is decomposed into the following terms:

$$E = E_{\text{bonded}} + \sum_{i<j} f_{ij}(E_{\text{elec}}(r_{ij}) + E_{\text{vdW}}(r_{ij})) \quad (1)$$

Here E_{bonded} is the bonded energy; E_{elec} is the electrostatic energy; and E_{vdW} is the van der Waals (vdW) energy. The factor (f_{ij}) is used to scale the nonbonded interactions (electrostatic and vdW terms) based on atom connectivity (0, 0.5 or 1). The electrostatic term is defined as

$$E_{\text{elec}}(r_{ij}) = \frac{q_i q_j e^2}{4\pi\epsilon_0 r_{ij}} \quad (2)$$

where q_i is the atomic charge assigned to atom i, and r_{ij} is interatomic distance. For ceramic materials, existing force fields[54,55] often employ a screening function to limit electrostatic interactions to short ranges. This approach, however, is incompatible with OPLS-AA and unsuitable for studying interfaces where long-range interactions play a significant role.[56−58] We therefore develop a force field for Li_6PS_5Cl that relies on bare electrostatics and assigns atomic charges explicitly (see eq 2). We then use the OPLS parameters for the polymer and Li_6PS_5Cl and develop a force field for their interface. The reference data used to generate the necessary

https://doi.org/10.1021/acsami.4c07440
ACS Appl. Mater. Interfaces XXXX, XXX, XXX−XXX

parameters for the ceramic and the polymer−ceramic systems are based on DFT calculations as outlined in the workflow of Figure 1.

2.1.1. Argyrodite: Li_6PS_5Cl. The total energy of the ceramic solid material is described by eq 1, where the electrostatic energy is defined in eq 2. We calculate atomic charges q_i in eq 2 using the density-derived electrostatic and chemical charge (DDEC) analysis[59,60] on the DFT-optimized Li_6PS_5Cl crystal structure (details included in the Supporting Information). The atoms in Li_6PS_5Cl are classified into five types (Li, P, S1, S2, Cl), where there are two sulfur atom types depending on whether they coordinate with phosphorus atoms (S1 or S2). The DDEC analysis incorporates both electron density and electrostatic terms to calculate atomic charges. The resulting charges are shown in Table S1. Notably, the charge for Li-ions in Li_6PS_5Cl is about +0.78, which is consistent with the practice of scaling the charge of ions when using the OPLS-AA force field (∼0.7−0.8) to correctly capture ion dynamics in polymer electrolyte systems.[61,62]

After charges are assigned, we determine the parameters for the E_{bonded} and E_{vdW} terms in eq 1 using the distribution function matching (DFM) approach, as done by Kobayashi and co-workers.[55] For Li_6PS_5Cl, we employ harmonic bond potentials for all bonded atom pairs, harmonic angle potential for the S1−P−S1 angle to preserve the PS_4 tetrahedral structure, and Born−Mayer−Huggins−Fumi−Tosi (BMHFT) potential[63,64] for the Li-X (X = S1, S2, Cl) vdW interactions (see the Supporting Information for details). In the DFM method, we first generate distribution functions from DFT-based MD simulations or DFT-MD to serve as the reference. Then, we optimize the parameters in the force field by fitting the calculated distribution using the force field model to the reference distribution. During this optimization process, the DFM approach also optimizes a term related to the stress tensor, such that the lattice cell parameters of the resulting force field agree with the DFT-MD reference. Representative radial distribution functions of Li-X pairs optimized using the DFM method are shown in Figure 2 (see Figure S2 for a complete set of distribution data). The resulting distributions calculated with our force field are in good agreement with the reference DFT results.

An important property that the Li_6PS_5Cl force field must capture for lithium battery studies is Li-ion diffusion. Li-ions diffuse fast in Li_6PS_5Cl, where the ionic conductivity is on the order of mS/cm at room temperature.[65−73] Previous experimental and computational studies have suggested that the site disorder of Cl^- and S^{2-} ions can significantly enhance Li-ion conductivity.[74−76] From our force field, we estimate the Li-ion diffusion coefficient to be 4.03×10^{-11} cm^2/s for the crystalline phase and 1.87×10^{-8} cm^2/s for the material with 50% disorder in Cl^- and S^{2-} sites (Figure S3). Our findings are consistent with values from previous DFT-MD studies: the Li-ion diffusion coefficient in Li_6PS_5Cl for its crystalline phase is around 10^{-11} cm^2/s,[77] and the diffusion coefficient increases with increased disorder in Cl^- and S^{2-} single anions, to around 10^{-7}−10^{-8} cm^2/s.[68,78,79] The computed diffusion coefficient of the disordered system is also consistent with experimental conductivity measurements.

2.1.2. Polymer−Argyrodite Interface. To parametrize the polymer−Li_6PS_5Cl interface model, we first find the lowest-energy surface structure of Li_6PS_5Cl from the bulk crystal structure using DFT, and then expose this ceramic surface to the polymer to create a polymer−solid interface (see Section 4.1). We then use the force field parameters from Li_6PS_5Cl and the polymer of interest to develop the additional parameters needed for the interface.

For a polymer−argyrodite interface system, the total energy (E_{tot}) is written as

$$E_{tot} = E_{polymer} + E_{solid} + E_{polymer-solid} \quad (3)$$

where each energy term represents the energy of each domain (the polymer and the solid), and the last term, $E_{polymer-solid}$, consists of intermolecular interactions between the atoms in the polymer and the solid domains. Each energy term is consistent with the OPLS-AA model (eq 1). In the $E_{polymer-solid}$ term, there are no bonded terms between the polymer and the solid domains, and eq 3 is rewritten as

$$E_{tot} = E_{elec} + E_{vdW,solid} + E_{bonded,solid} + E_{vdW,polymer} + E_{bonded,polymer} + E_{vdW,polymer-solid} \quad (4)$$

In this equation, parameters for the $E_{vdW,polymer}$ and $E_{bonded,polymer}$ terms are available from the existing OPLS-AA force field (e.g., see Section 4 in Supporting Information). Likewise, the atomic charges of the bulk polymer are also known from the OPLS-AA model. On the other hand, the creation of an interface may change the charge of ceramic atoms exposed to the surface in Li_6PS_5Cl due to surface polarization. To calculate the E_{elec} term in the presence of an interface, we carry out DDEC calculations of the Li_6PS_5Cl surface slab model. We find that the atomic charges of most atoms are nearly the same as their values in bulk Li_6PS_5Cl, and only the atoms exposed to the surface experience significant changes and degeneracy (see Table S1 in Supporting Information). Therefore, to model E_{elec} and the rest of the interaction among solid atom types in the presence of an interface ($E_{vdW,solid}$ and $E_{boned,solid}$), we use atomic charges calculated from the surface slab model but adapt the parameters for the bonded and vdW terms derived using the DFT data of bulk solid as described in Section 2.1.1.

The remaining unknown energy term in eq 4 is $E_{vdW,polymer-solid}$. The vdW term in OPLS-AA uses a Lennard-Jones (L-J) potential

$$E_{LJ}(r_{ij}) = 4\epsilon_{ij}\left[\left(\frac{\sigma_{ij}}{r_{ij}}\right)^{12} - \left(\frac{\sigma_{ij}}{r_{ij}}\right)^{6}\right] \quad (5)$$

where r_{ij} is the distance between atom i and atom j; ϵ_{ij} is the depth of the potential well; and σ_{ij} is the distance at which the potential energy is zero. The L-J parameters are obtained using the following combining rules:

$$\sigma_{ij} = \sqrt{\sigma_i \sigma_j} \quad (6)$$

$$\epsilon_{ij} = \sqrt{\epsilon_i \epsilon_j} \quad (7)$$

where the L-J parameters σ_i and ϵ_i are defined for each atom i.

To complete the interface model, we derive the L-J parameters for each atom type in the ceramic phase. In a previous report for a different ceramic−polymer system by Bonilla and co-workers,[48] L-J parameters for the interface are directly adapted from those in the solid force field. While their results are reasonable, we expect the atoms exposed on the solid surface to carry different polarization states than their bulk counterparts. Thus, we perform an interaction energy fitting approach to derive L-J parameters for solid atom types

https://doi.org/10.1021/acsami.4c07440
ACS Appl. Mater. Interfaces XXXX, XXX, XXX−XXX

in the presence of the polymer−solid interface using the combining rules in eqs 6 and 7.

A large data set of monomer conformations adsorbed to the Li_6PS_5Cl surface is collected with MD simulations for an initial set of trial L-J parameters. The interaction energy is defined as

$$\Delta E = E_{\text{solid+monomer}} - E_{\text{solid}} - E_{\text{monomer}} \quad (8)$$

where $E_{\text{solid+monomer}}$, E_{solid} and E_{monomer} are energies from three single-point DFT calculations of the corresponding separate systems. We repeat the calculation of interaction energies with the set of conformations sampled with iteratively refined trial force fields until they reach good agreement with those calculated from DFT. We cast this procedure as an optimization problem of minimizing the sum of the mean-squared deviation between the interaction energy from the trial force field and from DFT calculations. We consider monomers from polyethylene glycol (PEO), hydronated NBR (HNBR), and poly(vinylidene fluoride-*co*-hexafluoropropylene) (PVDF-HFP); the list of the monomers is summarized in Table S4. The final result from the least-squares fitting procedure is displayed in Figure 3, and the L-J parameter values are listed in Table S3. As seen in Figure 3, there is a good agreement between our force field and DFT across different monomers, suggesting good transferability of L-J parameters among the polymers reported in this study. Our computational framework outlined here (Figure 1) can be easily extended to develop force fields for other polymer−solid interface systems.

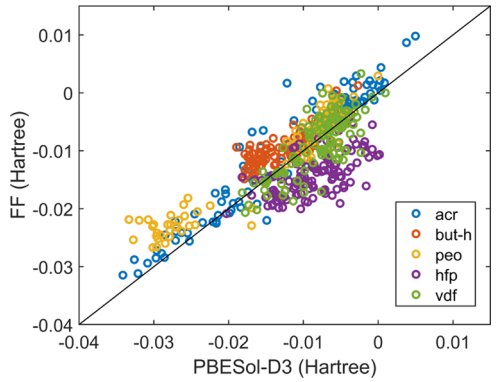

Figure 3. Results from the fitting of interaction energies for parametrization of LJ terms for the interaction between solid and polymer atom types at the interface. The different labels correspond to different monomers, and a full list of the corresponding chemical formulas is shown in Table S4. The optimized LJ parameters are listed in Table S3.

2.2. Free Energy Profile of Li-ion Across PEO/Li_6PS_5Cl Domain. We apply our newly developed ceramic/interface force field to investigate the energetics of Li-ion diffusion in the PEO/Li_6PS_5Cl composite system. We create two identical interfaces to model this system, as shown in Figure 4a. PEO chains adsorb onto the solid surface, forming a densely packed layer of adsorbed polymers approximately 5 Å thick at equilibrium. This adsorbed layer is illustrated by the peaks in the density profiles of carbon and oxygen atoms of PEO (Figure S5 of the Supporting Information). Note that ceramic Li-ions remain confined within the ceramic domain and do not cross the interface.

To understand the preference of Li-ions for the ceramic or polymeric domains, we conduct enhanced sampling simulations and determine the free energy profile of the ions across the polymer phase up to the ceramic surface. We use the *z*-coordinate of a single Li-ion as a collective variable and use the Adaptive Biasing Force method, where we apply biasing force along the direction perpendicular to the interfacial plane.[80] In Figure 4b, we plot the average free energy profile of surface Li-ions in a PEO/Li_6PS_5Cl composite system at 600 K. The *x*-axis represents the distance from the interface in the direction perpendicular to the interfacial plane, starting from the polymer−ceramic interface, traversing the polymer domain, and ending at the opposite polymer−ceramic interface. The free energy profile is perfectly symmetric, indicating that the vacancy created by the departing Li-ion is promptly filled by neighboring Li-ions. Previous studies of the bulk ceramic material have shown that this vacancy can migrate throughout the ceramic domain in a "string-like" motion in the solid.[75]

The collective free energy profile of Li-ions presented here is obtained by averaging over the profiles of all surface Li-ion sites. The free energy profiles of different Li-ions at the ceramic surface exhibit similar shapes and energy magnitudes, indicating that the specific location of a Li-ion on the surface has a minor influence on the thermodynamics (Figure S6 in the Supporting Information). An amorphous layer of Li-ions forms at the ceramic surface, as shown in Figure S7 in the Supporting Information. This finding is consistent with a previous report suggesting that polymer interactions with the ceramic domain lead to the formation of an amorphous layer of Li-ions at the ceramic surface.[48] This amorphous layer likely results in comparable free energy profiles for all surface Li-ions.

As seen in Figure 4b, the free energy minimum occurs at the interface, indicating that the Li-ions prefer to reside at the ceramic−polymer interface, rather than partitioning into the polymer domain. The free energy difference between the interface and the bulk polymer is approximately 14 k_BT, underscoring the small probability of finding Li-ions in the polymer. A local minimum is observed at around 5 Å away from each interface. This minimum is approximately $4k_BT$ lower than the bulk polymer region (see Figure 4b). As previously mentioned, PEO chains are densely packed near the interface (about 5 Å thick), creating an environment rich in oxygen atoms. Li-ions are primarily coordinated with the excess oxygens from PEO near the interface.[81]

Figure 4c shows the coordination motifs that arise for a Li-ion at three locations: the ceramic surface, the oxygen-dense region near the interface, and the polymer bulk. At the ceramic surface, the Li-ion is mainly coordinated with the sulfur atoms from the ceramic but also partially interacts with the oxygen atoms from the polymer, resulting in a coordination number of around three. As Li-ion migrates to the adsorbed polymer layer, it adopts a coordination structure similar to that in the polymer bulk, with a coordination number of around six (see Figure 4c). The Li-ion is fully coordinated in the polymer bulk by six oxygen atoms from the PEO chain.

We performed an additional free energy calculation to gain deeper insights into the source of the free energy difference between the interface and the polymer bulk. We inserted a Li-ion directly into the PEO domain (avoiding a vacancy formation in the ceramic domain) and smeared the extra positive charge across all phosphorus, sulfur, and chlorine atoms in the solid phase. We opted not to introduce a counterion to avoid changes in the Li-ion behavior. The free energy profile obtained after repeating the calculation with this inserted Li-ion is almost identical to that shown above (see Figure S8 of the Supporting Information). These results

https://doi.org/10.1021/acsami.4c07440
ACS Appl. Mater. Interfaces XXXX, XXX, XXX−XXX

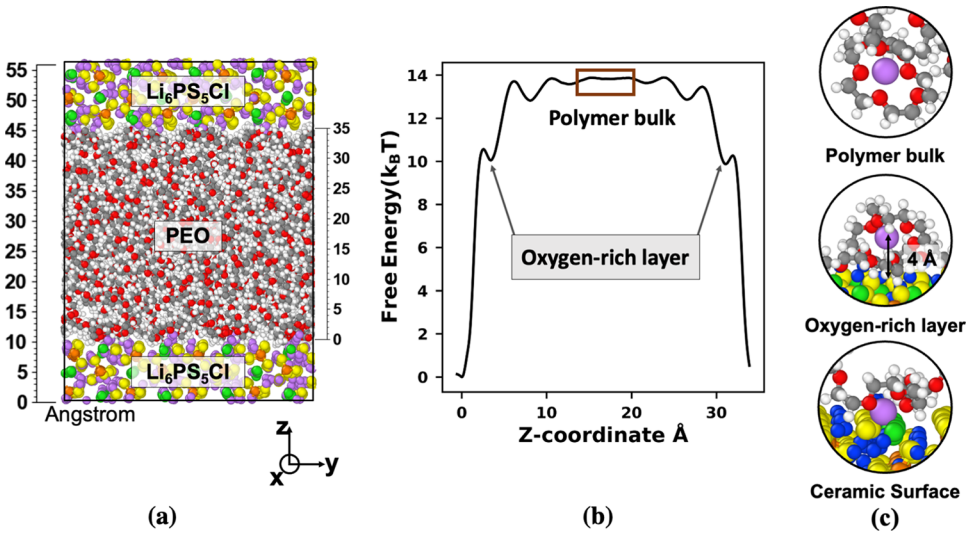

Figure 4. Li-ion free energy profile and coordination motifs. (a) Snapshot of the PEO/Li_6PS_5Cl composite system at 600 K, showing lithium (purple), sulfur (yellow), chloride (green), phosphorus (orange), oxygen (red), carbon (dark gray), and hydrogen (white). (b) Free energy profile of a Li-ion located on the ceramic surface as it travels through the polymer domain. The local minima in the profile correspond to the two distinct regions highlighted within the polymer domain (bulk vs oxygen-rich layer). (c) Coordination motifs of a Li-ion at three locations within the composite system: polymer bulk, oxygen-rich layer, and ceramic surface. The Li-ion of interest (or probe) is shown in purple, while other Li-ions in the ceramic are depicted in blue.

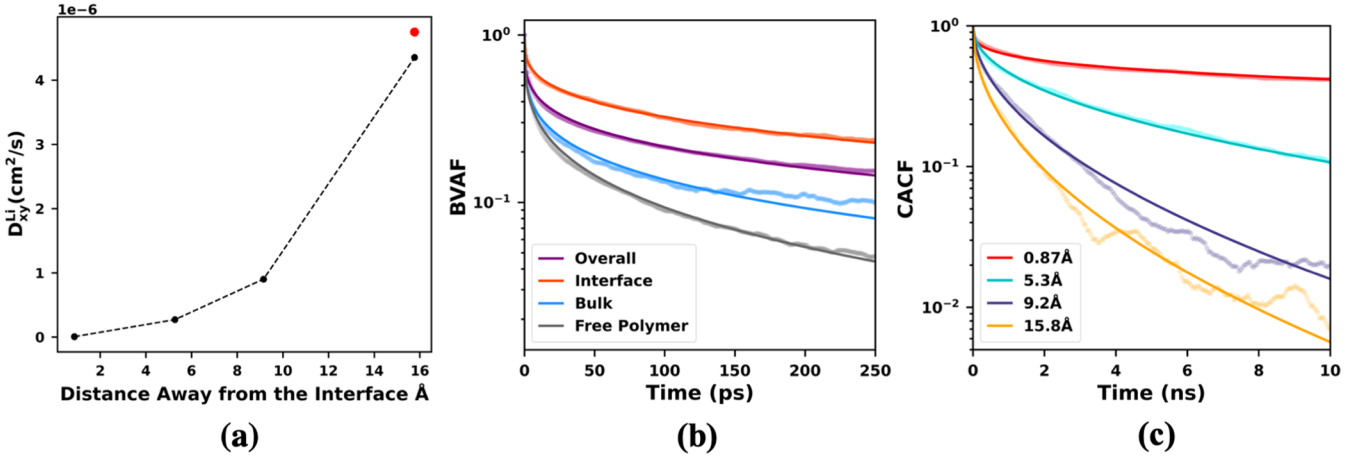

Figure 5. Characterization of single Li-ion diffusion at different distances from the ceramic surface. (a) Li-ion diffusivity versus distance from the interface. The diffusivity data for a single Li-ion in a bulk polymer melt is represented by a solid red dot, for reference. (b) Bond vector autocorrelation function of PEO backbone carbons and oxygens in the polymer domain of the composite system (interfacial region: blue; bulk region: green; overall: orange) and in free PEO melt in the absence of solid material (red). (c) Ion-hopping autocorrelation function of Li-ion at various distances from the interface. Note that the diffusivity data shown in (a) for the 0.87 and 5.3 Å cases correspond to apparent diffusivity. See Section S8 in the Supporting Information for a discussion of diffusivity calculations.

strongly suggest that the observed free energy difference originates from the stronger coordination interaction of Li-ion in the ceramic material compared to PEO. The free energy cost of merely creating a vacancy is minimal when compared to that of a Li-ion crossing the interface region.

2.3. Li-ion Transport in the PEO Domain. Thus, far, we have identified a substantial thermodynamic preference for Li-ions to remain in the ceramic phase compared to the polymer. We next consider whether any barriers arise for Li-ion transport parallel to the interfacial plane. We compute the two-dimensional (2D) planar diffusivity as a function of distance from the interface using eq 9 below:

$$D_{xy} = \frac{1}{4}\lim_{t\to\infty}\frac{\mathrm{d}}{\mathrm{d}t}\left(\frac{1}{N}\sum_{i=1}^{N}([\vec{r}_{x_i}(t) - \vec{r}_{x_i}(0)]^2 + [\vec{r}_{y_i}(t) - \vec{r}_{y_i}(0)]^2)\right) \quad (9)$$

We place Li-ions at different distances above the interface within the polymer by applying a harmonic restraining force on the ions in the z-direction (perpendicular to the interface). Figure 5a shows the planar diffusivity for different distances from the interface. The presence of the interface significantly slows down the Li-ion diffusion parallel to the interfacial plane. As a Li-ion moves away from the interface, its diffusivity increases considerably. Eventually, the 2D diffusivity ap-

https://doi.org/10.1021/acsami.4c07440
ACS Appl. Mater. Interfaces XXXX, XXX, XXX−XXX

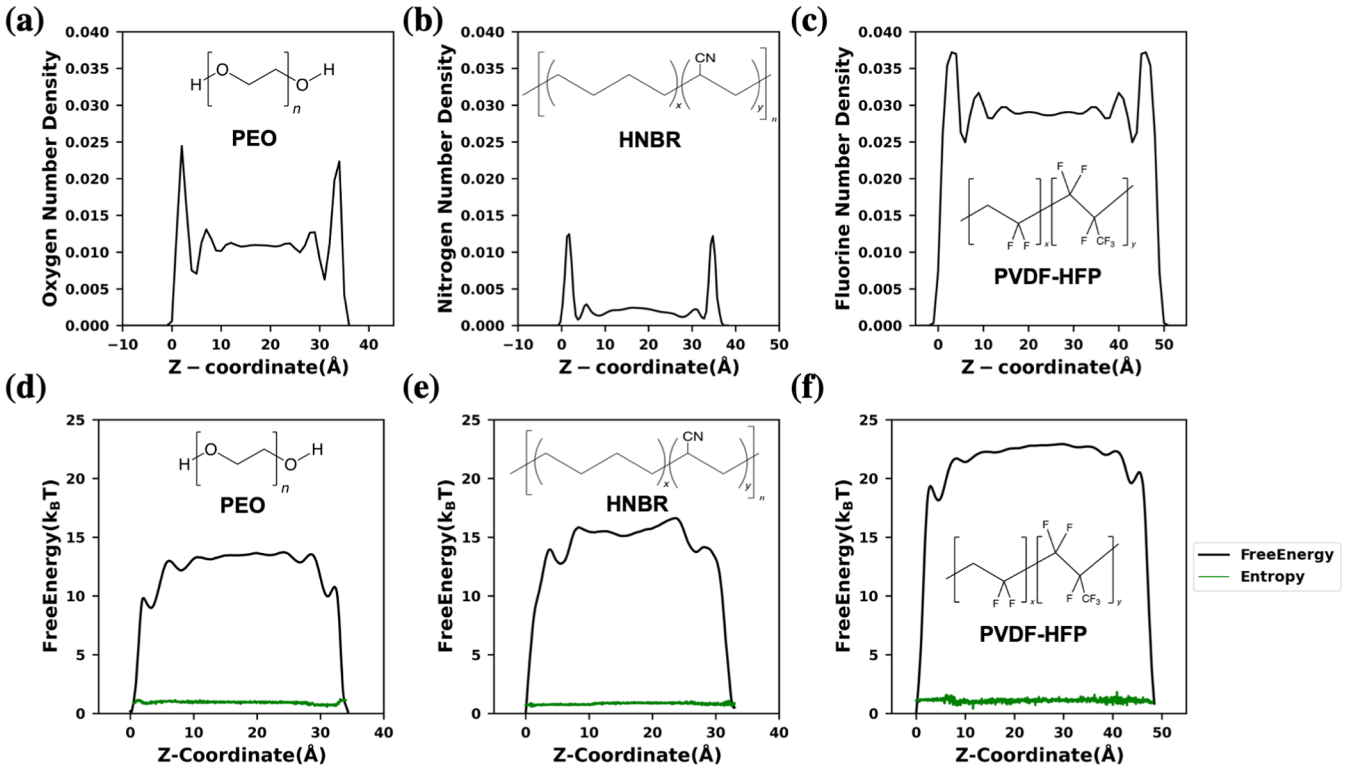

Figure 6. Li-ion free energy profiles in different polymer/Li_6PS_5Cl systems and number density profiles of electronegative atoms for the polymers. (a–c) Number density profiles of (a) oxygen atoms in PEO, (b) nitrogen atoms in HNBR, and (c) fluorine atoms in PVDF-HFP. (d–f) Li-ion Free Energy profiles, indicated by solid black lines, and entropic contribution, represented by green lines, in (d) PEO/Li_6PS_5Cl, (e) HNBR/Li_6PS_5Cl, and (f) PVDF-HFP/Li_6PS_5Cl systems.

proaches the bulk polymer value in the region furthest away from the interface. The diffusivity of Li-ion in the PEO bulk region is about 3 orders of magnitude higher than that at the interface. At a distance of approximately 16 Å from the interface, the dynamics of Li-ion are no longer affected by the presence of the interface (Figure S9 of the Supporting Information).

To understand this slowing-down effect near the interface, we now consider the differences in the polymer segmental mobility between the interfacial and bulk regions of the composite system. Figure 5b illustrates this difference using the bond-vector autocorrelation function (BVAF).[82] The BVAF measures how rapidly the bond vector between two adjoining backbone atoms forgets its initial orientation. PEO exhibits significantly slower segmental dynamics near the interface than in the bulk because PEO chains are adsorbed and packed more densely at the interface, which hinders their movement. The slower segmental mobility of PEO at the interface slows down Li-ion diffusion in this region. It is worth noting that, compared to the free PEO melt, PEO chains in the composite system display slower overall segmental mobility due to confinement effects introduced by the attractive solid surface.[83] The reduced segmental mobility explains the slightly reduced Li-ion diffusivity in the bulk region compared to that of a free PEO melt.

Previous studies have established that Li-ion diffusion in PEO melts depends on both polymer segmental dynamics and the frequency of ion hopping events.[30,52] To quantify the frequency of ion hopping events at various distances from the interface, we compute the ion hopping correlation function, denoted as CACF(t) (defined by eq 10). We fit the resulting correlation function to a stretched exponential equation of the form, $\mathrm{CACF}(f) = e^{-(\frac{t}{\tau})^{\beta}}$, where τ is the characteristic time and β is the stretching parameter. The results are presented in Figure 5c.

$$\mathrm{CACF}(f) = \frac{|S(t + t_0) \cap S(t_0)|}{|S(t_0)|} \tag{10}$$

In this equation, $S(t_0)$ represents the set of oxygen atoms from the PEO chain that coordinate with the Li-ion at time t_0, and $S(t + t_0)$ represents the set of oxygen atoms coordinated with the Li-ion at a later time $(t + t_0)$. $|\cdot|$ represents the number of members of a set. The correlation function captures the time it takes for a Li-ion to unbind from a polymer chain. This analysis allows us to compare the hopping rates at different distances from the interface. A faster decay of the correlation function indicates a higher number of ion-hopping events.[82]

As shown in Figure 5c, the correlation function exhibits little decay for Li-ions at the interface. This implies a low ion-hopping rate and a long characteristic time for a Li-ion to unbind from a polymer chain near the interface. There is a stabilizing force at the interface that effectively traps the Li-ion within its solvation shell. The ion hopping rates increase as the Li-ion moves away from the interface, indicating that this stabilizing force weakens gradually within the polymer domain over a distance of approximately 16 Å. Notably, the characteristic hopping time at the interface is roughly 50 times larger than that in the bulk polymer (see Table S6 in Supporting Information).

2.4. Comparison of Li-ion Transport in Various Polymer/Li_6PS_5Cl Interfacial Systems. To investigate the

https://doi.org/10.1021/acsami.4c07440
ACS Appl. Mater. Interfaces XXXX, XXX, XXX−XXX

influence of polymer materials on Li-ion transport, we analyzed the chemical environment and thermodynamics of ceramic−polymer interfaces for two additional polymer systems, HNBR and PVDF-HFP, alongside PEO. Unlike PEO, HNBR and PVDF-HFP are poor electrolytes, and there is an even smaller affinity by Li-ion to these materials due to weaker polymer−Li-ion interactions. For instance, HNBR coordinates with Li-ion primarily through the nitrogen atoms (coordination number ∼3). At the same time, PVDF-HFP barely interacts with Li-ion (see Figure S10 in Supporting Information).

In Figure 6a−c, we plot the density profile of the most electronegative atoms in each polymer (i.e., oxygen in PEO, nitrogen in HNBR, and fluorine in PVDF-HFP). The spatial profile of the number density in the polymer domain changes along the direction perpendicular to the interfacial plane. Notably, in all three systems, the number density profile peaks at a distance from the interface of around z = 5 Å and (L_z − 5) Å, where L_z is the thickness of the polymer layer (L_z = 35, 38, 50 Å for PEO, HBNR, and PBDF-HFP, respectively), indicating that there is an adsorbed layer of polymer chains with a high concentration of electronegative atoms. Moving toward the center of the polymer layer ($z = L_z/2$), we find that the density profile reaches a plateau value, corresponding to the bulk polymer density.

There is a strong correlation between the polymer interaction strength with Li-ions and the difference in the number density of the polymer bulk and near the interface. The difference in density shows a decreasing trend, PEO > HNBR > PVDF-HFP, indicating that PEO is packed more densely near the interface compared to HNBR and PVDF-HFP. This trend is the same as observed for the strength of interaction between Li-ions and electronegative atoms, as measured by the coordination number of Li-ions in the polymer melt. Interestingly, nitrogen atoms are more electronegative than oxygen atoms, but the concentration of nitrogen atoms in HNBR is low. Consequently, the overall interaction between HNBR and Li-ions at the interface is lower than that of PEO. In PVDF-HFP, the concentration of electronegative fluorine atoms is high, but the polymer exhibits the weakest interaction with Li-ion, resulting in smaller changes in the number density going from the polymer bulk to the interface. These results suggest that polymers undergo a conformational reorganization to a greater extent in response to the ceramic interface when they interact more strongly with the ceramic material and are more likely to solvate Li-ions.

In Figure 6d−f, we compare the Li-ion free energy profiles for the three polymers. There is a low solubility of Li-ions in all three cases, with all free energy differences being at least 10 k_BT. The shape of the free energy profiles is consistent with the corresponding density profiles. Like the PEO system (Figure 4b), local minima are also observed at ∼5 Å away from the interface in HNBR and PVDF-HFP, underscoring the presence of the densely packed polymer region.

The free energy difference between the polymer domain ($z = L_z/2$) and the middle of the interfacial region (z = 5 or L_z − 5 Å) remains high for all three polymers, about 5 k_BT. PEO system exhibits the lowest free energy difference, while the PVDF-HFP system shows the highest. We can explain this result by analyzing their respective coordination environments. As illustrated in Figure S10, PEO coordinates most favorably with Li-ion, forming a stable coordination shell comprising of 5−6 oxygen atoms, while PVDF-HFP coordinates the least with Li-ion, not showing any apparent coordination shell. Interestingly, the trend in their free energy differences (PBDF-HFP > HNBR > PEO) is strongly anticorrelated with the strength of the polymer−ion interaction near the ceramic surface (PBDF-HFP < HNBR < PEO), owing to the electronegative atoms. In other words, strong interactions between Li-ions and the electronegative atoms near the ceramic surface result in a low free energy for Li-ion solvation near the polymer−ceramic relative to that in the bulk polymer.

It is of interest to decompose the free energy entropic and enthalpic contributions, which are depicted by green lines in Figure 6d−f. Based on these plots, the entropic contributions to the Li-ion free energy are approximately the same for all three systems, with a value of around ∼3 k_BT, and remain nearly constant along the direction perpendicular to the interface. These findings suggest that the spatial variation in the Li-ion free energy profile among different polymeric systems is primarily due to enthalpy, which is dominated by the electrostatic and vdW interactions between Li-ions and the electronegative atoms in the polymers. Note that our free energy calculations correspond to a dilute Li-ion concentration (single Li-ion), and entropy could be more important for larger concentrations.

3. CONCLUSIONS

Polymer−ceramic composite solid-state electrolytes hold promise for applications in energy storage. In this work, we have presented a detailed study of Li-ion thermodynamics and dynamics across the polymeric phase in a composite system, starting at the ceramic phase. To that end, we developed a force field for argyrodite-polymeric composites that is consistent with the OPLS-AA force field for liquids and polymers. With this new force field, we carried out large-scale, long time-scale MD simulations of the free energy and transport of Li-ions for several polymeric materials of interest for energy storage, including PEO/Li_6PS_5Cl, HNBR/Li_6PS_5Cl, and PVDF-HFP/Li_6PS_5Cl.

Free energy calculations have provided a number of previously unavailable insights into the solvation of Li-ions in the polymer phase near the ceramic phase. First, the free energy difference between the argyrodite interface and the bulk polymer is approximately 14 k_BT for PEO, increasing to 19 and 22 k_BT for HNBR and PVDF-HFP, respectively. Second, the entropic contribution to the free energy difference is similar across all polymers, and has a value of approximately 3 k_BT, showing that the differences in their respective free energies is largely due to the energetic aspects of Li-ion−polymer interactions. The three polymers considered here form a dense layer of electronegative atoms at approximately 5 Å from the interface. Polymers in this layer tend to solvate Li-ions, leading to a local free energy minimum along the direction perpendicular to the interface plane. The effect of the ceramic phase on the Li-ion solvation is felt over a distance of approximately 15 Å from the interface; solvation by the polymer assumes a bulk value behavior after that.

The diffusivity of Li-ion in the polymer is significantly smaller near the interface than in the bulk polymer. This reduced diffusivity is attributed to the slower segmental dynamics of the polymer near the interface, as revealed by the bond vector autocorrelation function for the polymers and by an analysis of Li-ion hopping near the interface and in the bulk. Several studies have shown that polymer segmental mobility has a significant impact on ion diffusion.[82,84,85] Our results indicate that once Li-ions from the ceramic phase reach

https://doi.org/10.1021/acsami.4c07440
ACS Appl. Mater. Interfaces XXXX, XXX, XXX−XXX

the polymer−ceramic interface, Li-ions are likely to be trapped there or in a nearby minimum provided by a densely packed polymer layer at the solid surface, consistent with recent experiments.[86]

Our results all together paint a picture of the argyrodite interface where Li-ion transport primarily occurs within the ceramic. Transport across the polymeric material is hindered by significant thermodynamic barriers, even for a relatively good polymer electrolyte such as PEO. Local minima arise in the free energy profile for all three polymers studied, corresponding to favorable coordination environments created by the adsorbed polymer layers near the interface. Taken together, our results show that improvements in composite electrolyte systems can be made by (1) reducing the free energy difference between the polymer and the ceramic materials by providing a better solvation environment for Li-ions, (2) providing an optimized interaction between the polymer and ceramic that leads to local free energy minima in the interfacial region, through design of new polymers and functionalization of the interfaces, and (3) facilitating ion transport in the polymer by designing materials with higher segmental mobility and lower glass transition temperatures.

4. COMPUTATIONAL METHODS

4.1. Polymer/Ceramic Force Field Development. In the parametrization of the ceramic force field, we apply a modified distribution function matching (DFM) approach.[55] To obtain the reference distribution for the ceramic phase, we carry out DFT-MD simulations with CP2K ver. 7.1 package.[87] We use the cubic structure of Li_6PS_5Cl, obtained from the Materials Project[88] (project number mp-985592). The solid is described as a 2 × 2 × 2 supercell, consisting of 416 atoms. DFT-MD simulations as Born−Oppenheimer molecular dynamics using PBESol as the exchange−correlational functional,[89] the Goedecker−Tetter−Hutter pseudopotentials to describe ionic cores,[90−92] and DZVP-MOLOPT-SR to describe valence electrons.[93] We used a multigrid cutoff of 550 Ry, a relative cutoff of 60 Ry, and a time step of 1.0 fs. A Nose-Hoover thermostat[94,95] is applied to control the temperature at 300 K with a time constant of 100 fs. The system is equilibrated at constant pressure and temperature (NPT ensemble) for 3 ps (ps), followed by a production run at constant volume and temperature (NVT ensemble). The reference distribution data converged within 1 ps (see Figure S1). Additional details of the parametrization protocol of the solid force field are provided in the Supporting Information.

We construct the ceramic surface slab model used in this work by minimizing the surface energy of a symmetric slab of Li_6PS_5Cl using DFT. The slab model was generated using the algorithm by Sun et al.[96] as implemented in the Pymatgen package.[97] The $F\bar{4}3m$ (110) surface with Li−S−Cl termination was found to be the most stable. Thus, this surface model is used as a reference to create the ceramic force field. Additional details are provided in the Supporting Information. To obtain L-J parameters for the interactions between the solid and the polymer phases, we calculate the interaction energy between a monomer and the ceramic surface from the force field with trial parameters (see eq 8) and fit the energy to that from DFT. A differential evolution method[98−100] is used to minimize the mean-squared deviation between the trial and the reference data. Additional details on this parametrization are provided in the Supporting Information.

4.2. Molecular Dynamics Simulations Using the Polymer−Ceramic Force Field. MD simulations of composite systems are performed using LAMMPS.[101] Atomic partial charges and force field parameters for HNBR are taken from Molinari et al.[102] The fluoroalkyl parameters are taken from Watkins et al.[103] All other polymers are modeled using the OPLS-AA force field.[53] The fluorine atomic charges are reparameterized based on our DFT calculations and are validated against experimental data. (Section 4 in the Supporting Information) All other atomic charges in the polymers are from the original OPLS-AA model and are assigned based on their atom types. Force field parameters for all three polymers—PEO, HNBR, and PVDF-HFP—were validated against experimental data (Table S5 in the Supporting Information). A Velocity Verlet integrator with a 1 fs time step is used in all MD simulations. van der Waals interactions are evaluated with a cutoff distance of 11 Å. Coulomb interactions are estimated using a particle−particle particle-mesh (PPPM) solver with a cutoff distance of 11 Å.[104] Three-dimensional periodic boundary conditions are applied. Additional details of the simulation protocol are provided in the Supporting Information.

■ ASSOCIATED CONTENT

Supporting Information

The Supporting Information is available free of charge at https://pubs.acs.org/doi/10.1021/acsami.4c07440.

Additional discussions on solid force field development; construction of stable solid surface structure; interface interaction force field development; MD simulation protocol; number density profile of the composite system; free energy profile calculations; diffusion coefficient calculations; BVAF calculations; polymer RDFs (PDF)

Chemical structure of the stable surface (XYZ)

■ AUTHOR INFORMATION

Corresponding Author

Juan J. de Pablo − *Pritzker School of Molecular Engineering, University of Chicago, Chicago, Illinois 60637, United States;* orcid.org/0000-0002-3526-516X; Email: depablo@uchicago.edu

Authors

Yuxi Chen − *Pritzker School of Molecular Engineering, University of Chicago, Chicago, Illinois 60637, United States*

Dongyue Liang − *Pritzker School of Molecular Engineering, University of Chicago, Chicago, Illinois 60637, United States*

Elizabeth M. Y. Lee − *Department of Materials Science and Engineering, University of California, Irvine, California 92697, United States;* orcid.org/0000-0001-9143-3140

Sokseiha Muy − *Theory and Simulations of Materials (THEOS) and National Centre for Computational Design and Discovery of Novel Materials (MARVEL), École Polytechnique Fédérale de Lausanne, CH-1015 Lausanne, Switzerland;* orcid.org/0000-0001-6457-9187

Maxime Guillaume − *Syensqo R&I, 1120 Brussels, Belgium*

Marc-David Braida − *Syensqo R&I, 93300 Aubervilliers, France*

Antoine A. Emery − *Syensqo R&I, 1120 Brussels, Belgium*

Nicola Marzari − *Theory and Simulations of Materials (THEOS) and National Centre for Computational Design and Discovery of Novel Materials (MARVEL), École Polytechnique Fédérale de Lausanne, CH-1015 Lausanne, Switzerland;* orcid.org/0000-0002-9764-0199

Complete contact information is available at: https://pubs.acs.org/10.1021/acsami.4c07440

Author Contributions

▽Y.C. and D.L. contributed equally to this work.

Notes

The authors declare no competing financial interest.

https://doi.org/10.1021/acsami.4c07440
ACS Appl. Mater. Interfaces XXXX, XXX, XXX−XXX

■ ACKNOWLEDGMENTS

The authors are grateful to Syensqo for financial support. We gratefully acknowledge the use of the computational resources at the University of Chicago's Research Computing Center (RCC) and the use of Bebop in the Laboratory Computing Resource Center at Argonne National Laboratory. The development of advanced sampling codes for the free energy calculations reported here was supported by the Department of Energy, Basic Energy Sciences, through the Midwest Integrated Center for Computational Materials (MICCoM).

■ REFERENCES

(1) Carrasco, J. M.; Franquelo, L. G.; Bialasiewicz, J. T.; Galván, E.; PortilloGuisado, R. C.; Prats, M. M.; León, J. I.; Moreno-Alfonso, N. Power-electronic systems for the grid integration of renewable energy sources: A survey. *IEEE Trans. Ind. Electron.* **2006**, *53*, 1002−1016.

(2) Beaudin, M.; Zareipour, H.; Schellenberglabe, A.; Rosehart, W. Energy storage for mitigating the variability of renewable electricity sources: An updated review. *Energy Sustainable Dev.* **2010**, *14*, 302−314.

(3) Cheng, X.-B.; Zhang, R.; Zhao, C.-Z.; Zhang, Q. Toward safe lithium metal anode in rechargeable batteries: a review. *Chem. Rev.* **2017**, *117*, 10403−10473.

(4) Palacín, M. R.; de Guibert, A. Why do batteries fail? *Science* **2016**, *351*, No. 1253292.

(5) Chen, Y.; Lee, E. M.; Gil, P. S.; Ma, P.; Amanchukwu, C. V.; de Pablo, J. J. Molecular engineering of fluoroether electrolytes for lithium metal batteries. *Mol. Syst. Des. Eng.* **2023**, *8*, 195−206.

(6) Janek, J.; Zeier, W. G. A solid future for battery development. *Nat. Energy* **2016**, *1*, 1−4.

(7) Zhao, Q.; Stalin, S.; Zhao, C.-Z.; Archer, L. A. Designing solid-state electrolytes for safe, energy-dense batteries. *Nat. Rev. Mater.* **2020**, *5*, 229−252.

(8) Bachman, J. C.; Muy, S.; Grimaud, A.; Chang, H.-H.; Pour, N.; Lux, S. F.; Paschos, O.; Maglia, F.; Lupart, S.; Lamp, P.; et al. Inorganic solid-state electrolytes for lithium batteries: mechanisms and properties governing ion conduction. *Chem. Rev.* **2016**, *116*, 140−162.

(9) Wang, S.; Xu, H.; Li, W.; Dolocan, A.; Manthiram, A. Interfacial chemistry in solid-state batteries: formation of interphase and its consequences. *J. Am. Chem. Soc.* **2018**, *140*, 250−257.

(10) Li, Y.; Xu, B.; Xu, H.; Duan, H.; Lü, X.; Xin, S.; Zhou, W.; Xue, L.; Fu, G.; Manthiram, A.; Goodenough, J. B. Hybrid polymer/garnet electrolyte with a small interfacial resistance for lithium-ion batteries. *Angew. Chem., Int. Ed.* **2017**, *56*, 753−756.

(11) Dong, D.; Zhou, B.; Sun, Y.; Zhang, H.; Zhong, G.; Dong, Q.; Fu, F.; Qian, H.; Lin, Z.; Lu, D.; et al. Polymer electrolyte glue: A universal interfacial modification strategy for all-solid-state Li batteries. *Nano Lett.* **2019**, *19*, 2343−2349.

(12) Jiang, Y.; Yan, X.; Ma, Z.; Mei, P.; Xiao, W.; You, Q.; Zhang, Y. Development of the PEO based solid polymer electrolytes for all-solid state lithium ion batteries. *Polymers* **2018**, *10*, No. 1237.

(13) Pożyczka, K.; Marzantowicz, M.; Dygas, J.; Krok, F. Ionic conductivity and lithium transference number of poly (ethylene oxide): LiTFSI system. *Electrochim. Acta* **2017**, *227*, 127−135.

(14) Xue, Z.; He, D.; Xie, X. Poly (ethylene oxide)-based electrolytes for lithium-ion batteries. *J. Mater. Chem. A* **2015**, *3*, 19218−19253.

(15) Chen, L.; Huang, S.; Ma, D.; Xiong, Y.; Qiu, J.; Cao, G.; Zhang, H. Stabilizing Ceramic-Based Electrolyte Interfaces with Self-Viscous Modification Strategy for Solid-State Lithium Batteries. *Energy Fuels* **2021**, *35*, 13411−13418.

(16) Kumar, B.; Scanlon, L. G. Polymer-ceramic composite electrolytes. *J. Power Sources* **1994**, *52*, 261−268.

(17) Kumar, B.; Scanlon, L. G. Polymer−ceramic composite electrolytes: conductivity and thermal history effects. *Solid State Ionics* **1999**, *124*, 239−254.

(18) Kumar, B.; Scanlon, L. G.; Spry, R. J. On the origin of conductivity enhancement in polymer-ceramic composite electrolytes. *J. Power Sources* **2001**, *96*, 337−342.

(19) Wan, Z.; Lei, D.; Yang, W.; Liu, C.; Shi, K.; Hao, X.; Shen, L.; Lv, W.; Li, B.; Yang, Q.-H.; et al. Low resistance-integrated all-solid-state battery achieved by Li7La3Zr2O12 nanowire upgrading polyethylene oxide (PEO) composite electrolyte and PEO cathode binder. *Adv. Funct. Mater.* **2019**, *29*, No. 1805301.

(20) Gorecki, W.; Jeannin, M.; Belorizky, E.; Roux, C.; Armand, M. Physical properties of solid polymer electrolyte PEO (LiTFSI) complexes. *J. Phys.: Condens. Matter* **1995**, *7*, No. 6823.

(21) Liu, P.; Counihan, M. J.; Zhu, Y.; Connell, J. G.; Sharon, D.; Patel, S. N.; Redfern, P. C.; Zapol, P.; Markovic, N. M.; Nealey, P. F.; et al. Increasing ionic conductivity of poly (ethylene oxide) by reaction with metallic Li. *Adv. Energy Sustainability Res.* **2022**, *3*, No. 2100142.

(22) Devaux, D.; Bouchet, R.; Glé, D.; Denoyel, R. Mechanism of ion transport in PEO/LiTFSI complexes: Effect of temperature, molecular weight and end groups. *Solid State Ionics* **2012**, *227*, 119−127.

(23) Park, J.-S.; Jo, C.-H.; Myung, S.-T. Comprehensive Understanding on Lithium Argyrodite Electrolytes for Stable and Safe All-Solid-State Lithium Batteries. *Energy Storage Mater.* **2023**, *61*, No. 102869.

(24) Pang, B.; Gan, Y.; Xia, Y.; Huang, H.; He, X.; Zhang, W. Regulation of the interfaces between argyrodite solid electrolytes and lithium metal anode. *Front. Chem.* **2022**, *10*, No. 837978.

(25) Wenzel, S.; Sedlmaier, S. J.; Dietrich, C.; Zeier, W. G.; Janek, J. Interfacial reactivity and interphase growth of argyrodite solid electrolytes at lithium metal electrodes. *Solid State Ionics* **2018**, *318*, 102−112.

(26) Simon, F. J.; Hanauer, M.; Henss, A.; Richter, F. H.; Janek, J. Properties of the interphase formed between argyrodite-type Li6PS5Cl and polymer-based PEO10: LiTFSI. *ACS Appl. Mater. Interfaces* **2019**, *11*, 42186−42196.

(27) Dixit, M.; Muralidharan, N.; Parejiya, A.; Jafta, C.; Du, Z.; Neumayer, S. M.; Essehli, R.; Amin, R.; Balasubramanian, M.; Belharouak, I. Differences in the Interfacial Mechanical Properties of Thiophosphate and Argyrodite Solid Electrolytes and Their Composites. *ACS Appl. Mater. Interfaces* **2022**, *14*, 44292−44302.

(28) Simon, F. J.; Hanauer, M.; Richter, F. H.; Janek, J. Interphase formation of PEO20: LiTFSI-Li6PS5Cl composite electrolytes with lithium metal. *ACS Appl. Mater. Interfaces* **2020**, *12*, 11713−11723.

(29) Fong, K. D.; Self, J.; Diederichsen, K. M.; Wood, B. M.; McCloskey, B. D.; Persson, K. A. Ion transport and the true transference number in nonaqueous polyelectrolyte solutions for lithium ion batteries. *ACS Cent. Sci.* **2019**, *5*, 1250−1260.

(30) Webb, M. A.; Savoie, B. M.; Wang, Z.-G.; Miller, T. F., III Chemically specific dynamic bond percolation model for ion transport in polymer electrolytes. *Macromolecules* **2015**, *48*, 7346−7358.

(31) Heinz, H.; Ramezani-Dakhel, H. Simulations of inorganic-bioorganic interfaces to discover new materials: insights, comparisons to experiment, challenges, and opportunities. *Chem. Soc. Rev.* **2016**, *45*, 412−448.

(32) Dhakane, A.; Varshney, V.; Liu, J.; Heinz, H.; Jain, A. Molecular dynamics simulations of separator-cathode interfacial thermal transport in a Li-ion cell. *Surf. Interfaces* **2020**, *21*, No. 100674.

(33) Lourenço, T. C.; Zhang, Y.; Costa, L. T.; Maginn, E. J. A molecular dynamics study of lithium-containing aprotic heterocyclic ionic liquid electrolytes. *J. Chem. Phys.* **2018**, *148*, No. 193834.

(34) Webb, M. A.; Jung, Y.; Pesko, D. M.; Savoie, B. M.; Yamamoto, U.; Coates, G. W.; Balsara, N. P.; Wang, Z.-G.; Miller, T. F., III Systematic computational and experimental investigation of lithium-ion transport mechanisms in polyester-based polymer electrolytes. *ACS Cent. Sci.* **2015**, *1*, 198−205.

(35) Sharon, D.; Bennington, P.; Webb, M. A.; Deng, C.; De Pablo, J. J.; Patel, S. N.; Nealey, P. F. Molecular level differences in ionic solvation and transport behavior in ethylene oxide-based homopol-

https://doi.org/10.1021/acsami.4c07440
ACS Appl. Mater. Interfaces XXXX, XXX, XXX−XXX

ymer and block copolymer electrolytes. *J. Am. Chem. Soc.* **2021**, *143*, 3180−3190.
(36) Bennington, P.; Deng, C.; Sharon, D.; Webb, M. A.; de Pablo, J. J.; Nealey, P. F.; Patel, S. N. Role of solvation site segmental dynamics on ion transport in ethylene-oxide based side-chain polymer electrolytes. *J. Mater. Chem. A* **2021**, *9*, 9937−9951.
(37) Cui, Q.; Hernandez, R.; Mason, S. E.; Frauenheim, T.; Pedersen, J. A.; Geiger, F. Sustainable nanotechnology: opportunities and challenges for theoretical/computational studies. *J. Phys. Chem. B* **2016**, *120*, 7297−7306.
(38) Dasetty, S.; Meza-Morales, P. J.; Getman, R. B.; Sarupria, S. Simulations of interfacial processes: recent advances in force field development. *Curr. Opin. Chem. Eng.* **2019**, *23*, 138−145.
(39) Heinz, H.; Lin, T.-J.; Kishore Mishra, R.; Emami, F. S. Thermodynamically consistent force fields for the assembly of inorganic, organic, and biological nanostructures: the INTERFACE force field. *Langmuir* **2013**, *29*, 1754−1765.
(40) Vanommeslaeghe, K.; Hatcher, E.; Acharya, C.; Kundu, S.; Zhong, S.; Shim, J.; Darian, E.; Guvench, O.; Lopes, P.; Vorobyov, I.; Mackerell, A. D. CHARMM general force field: A force field for drug-like molecules compatible with the CHARMM all-atom additive biological force fields. *J. Comput. Chem.* **2010**, *31*, 671−690.
(41) MacKerell, A. D., Jr; Banavali, N.; Foloppe, N. Development and current status of the CHARMM force field for nucleic acids. *Biopolymers* **2000**, *56*, 257−265.
(42) Wang, J.; Wolf, R. M.; Caldwell, J. W.; Kollman, P. A.; Case, D. A. Development and testing of a general amber force field. *J. Comput. Chem.* **2004**, *25*, 1157−1174.
(43) Robertson, M. J.; Tirado-Rives, J.; Jorgensen, W. L. Improved peptide and protein torsional energetics with the OPLS-AA force field. *J. Chem. Theory Comput.* **2015**, *11*, 3499−3509.
(44) Robertson, M. J.; Qian, Y.; Robinson, M. C.; Tirado-Rives, J.; Jorgensen, W. L. Development and Testing of the OPLS-AA/M Force Field for RNA. *J. Chem. Theory Comput.* **2019**, *15*, 2734−2742.
(45) Kim, J.-S.; Jung, W. D.; Son, J.-W.; Lee, J.-H.; Kim, B.-K.; Chung, K.-Y.; Jung, H.-G.; Kim, H. Atomistic assessments of lithium-ion conduction behavior in glass-ceramic lithium thiophosphates. *ACS Appl. Mater. Interfaces* **2019**, *11*, 13−18.
(46) Dawson, J. A. Going against the Grain: Atomistic Modeling of Grain Boundaries in Solid Electrolytes for Solid-State Batteries. *ACS Mater. Au* **2024**, *4*, 1−13.
(47) Liang, D.; Liu, J.; Heinz, H.; Mason, S. E.; Hamers, R. J.; Cui, Q. Binding of polar and hydrophobic molecules at the LiCoO 2 (001)-water interface: force field development and molecular dynamics simulations. *Nanoscale* **2022**, *14*, 7003−7014.
(48) Bonilla, M. R.; García Daza, F. A.; Ranque, P.; Aguesse, F.; Carrasco, J.; Akhmatskaya, E. Unveiling interfacial Li-Ion dynamics in Li7La3Zr2O12/PEO (LiTFSI) composite polymer-ceramic solid electrolytes for all-solid-state lithium Batteries. *ACS Appl. Mater. Interfaces* **2021**, *13*, 30653−30667.
(49) Li, Y.; Arnold, W.; Thapa, A.; Jasinski, J. B.; Sumanasekera, G.; Sunkara, M.; Druffel, T.; Wang, H. Stable and flexible sulfide composite electrolyte for high-performance solid-state lithium batteries. *ACS Appl. Mater. Interfaces* **2020**, *12*, 42653−42659.
(50) Ma, D.; Chen, L.; Li, Y.; Liu, Y.; Zhang, H.; Wang, B. Asymmetric polymer solid electrolyte constructed by dopamine-modified Li1. 4Al0. 4Ti1. 6 (PO4) 3 for dendrite-free lithium battery. *Ionics* **2022**, *28*, 2693−2700.
(51) Deng, C.; Bennington, P.; Sánchez-Leija, R. J.; Patel, S. N.; Nealey, P. F.; de Pablo, J. J. Entropic Penalty Switches Li+ Solvation Site Formation and Transport Mechanisms in Mixed Polarity Copolymer Electrolytes. *Macromolecules* **2023**, *56*, 8069−8079.
(52) Deng, C.; Webb, M. A.; Bennington, P.; Sharon, D.; Nealey, P. F.; Patel, S. N.; De Pablo, J. J. Role of molecular architecture on ion transport in ethylene oxide-based polymer electrolytes. *Macromolecules* **2021**, *54*, 2266−2276.
(53) Jorgensen, W. L.; Maxwell, D. S.; Tirado-Rives, J. Development and testing of the OPLS all-atom force field on conformational energetics and properties of organic liquids. *J. Am. Chem. Soc.* **1996**, *118*, 11225−11236.
(54) Adams, S.; Rao, R. P. Structural requirements for fast lithium ion migration in Li 10 GeP 2 S 12. *J. Mater. Chem.* **2012**, *22*, 7687−7691.
(55) Kobayashi, R.; Miyaji, Y.; Nakano, K.; Nakayama, M. High-throughput production of force-fields for solid-state electrolyte materials. *APL Mater.* **2020**, *8*, No. 081111.
(56) Suchorski, Y.; Kozlov, S. M.; Bespalov, I.; Datler, M.; Vogel, D.; Budinska, Z.; Neyman, K. M.; Rupprechter, G. The role of metal/oxide interfaces for long-range metal particle activation during CO oxidation. *Nat. Mater.* **2018**, *17*, 519−522.
(57) French, R. H.; Parsegian, V. A.; Podgornik, R.; Rajter, R. F.; Jagota, A.; Luo, J.; Asthagiri, D.; Chaudhury, M. K.; Chiang, Y.-m.; Granick, S.; et al. Long range interactions in nanoscale science. *Rev. Mod. Phys.* **2010**, *82*, No. 1887.
(58) Pham, T. A.; Ping, Y.; Galli, G. Modelling heterogeneous interfaces for solar water splitting. *Nat. Mater.* **2017**, *16*, 401−408.
(59) Manz, T. A.; Sholl, D. S. Improved atoms-in-molecule charge partitioning functional for simultaneously reproducing the electrostatic potential and chemical states in periodic and nonperiodic materials. *J. Chem. Theory Comput.* **2012**, *8*, 2844−2867.
(60) Manz, T. A.; Sholl, D. S. Chemically meaningful atomic charges that reproduce the electrostatic potential in periodic and nonperiodic materials. *J. Chem. Theory Comput.* **2010**, *6*, 2455−2468.
(61) Mogurampelly, S.; Ganesan, V. Structure and mechanisms underlying ion transport in ternary polymer electrolytes containing ionic liquids. *J. Chem. Phys.* **2017**, *146*, No. 074902.
(62) Costa, L. T.; Sun, B.; Jeschull, F.; Brandell, D. Polymer-ionic liquid ternary systems for Li-battery electrolytes: Molecular dynamics studies of LiTFSI in a EMIm-TFSI and PEO blend. *J. Chem. Phys.* **2015**, *143*, No. 024904.
(63) Fumi, F.; Tosi, M. Ionic sizes and born repulsive parameters in the NaCl-type alkali halides—I: The Huggins-Mayer and Pauling forms. *J. Phys. Chem. Solids* **1964**, *25*, 31−43.
(64) Tosi, M.; Fumi, F. Ionic sizes and born repulsive parameters in the NaCl-type alkali halides—II: The generalized Huggins-Mayer form. *J. Phys. Chem. Solids* **1964**, *25*, 45−52.
(65) Adeli, P.; Bazak, J. D.; Huq, A.; Goward, G. R.; Nazar, L. F. Influence of aliovalent cation substitution and mechanical compression on Li-ion conductivity and diffusivity in argyrodite solid electrolytes. *Chem. Mater.* **2021**, *33*, 146−157.
(66) Wang, S.; Zhang, Y.; Zhang, X.; Liu, T.; Lin, Y.-H.; Shen, Y.; Li, L.; Nan, C.-W. High-conductivity argyrodite Li6PS5Cl solid electrolytes prepared via optimized sintering processes for all-solid-state lithium-sulfur batteries. *ACS Appl. Mater. Interfaces* **2018**, *10*, 42279−42285.
(67) Boulineau, S.; Courty, M.; Tarascon, J.-M.; Viallet, V. Mechanochemical synthesis of Li-argyrodite Li6PS5X (X= Cl, Br, I) as sulfur-based solid electrolytes for all solid state batteries application. *Solid State Ionics* **2012**, *221*, 1−5.
(68) Yu, C.; Ganapathy, S.; De Klerk, N. J.; Roslon, I.; van Eck, E. R.; Kentgens, A. P.; Wagemaker, M. Unravelling li-ion transport from picoseconds to seconds: bulk versus interfaces in an argyrodite li6ps5cl-li2s all-solid-state li-ion battery. *J. Am. Chem. Soc.* **2016**, *138*, 11192−11201.
(69) Zhang, J.; Zhong, H.; Zheng, C.; Xia, Y.; Liang, C.; Huang, H.; Gan, Y.; Tao, X.; Zhang, W. All-solid-state batteries with slurry coated LiNi0. 8Co0. 1Mn0. 1O2 composite cathode and Li6PS5Cl electrolyte: Effect of binder content. *J. Power Sources* **2018**, *391*, 73−79.
(70) Zhang, Z.; Zhang, L.; Liu, Y.; Yu, C.; Yan, X.; Xu, B.; Wang, L.-m. Synthesis and characterization of argyrodite solid electrolytes for all-solid-state Li-ion batteries. *J. Alloys Compd.* **2018**, *747*, 227−235.
(71) Yu, C.; Ganapathy, S.; Hageman, J.; Van Eijck, L.; Van Eck, E. R.; Zhang, L.; Schwietert, T.; Basak, S.; Kelder, E. M.; Wagemaker, M. Facile synthesis toward the optimal structure-conductivity characteristics of the argyrodite Li6PS5Cl solid-state electrolyte. *ACS Appl. Mater. Interfaces* **2018**, *10*, 33296−33306.

https://doi.org/10.1021/acsami.4c07440
ACS Appl. Mater. Interfaces XXXX, XXX, XXX−XXX

(72) Rajagopal, R.; Subramanian, Y.; Jung, Y. J.; Kang, S.; Ryu, K.-S. Rapid Synthesis of Highly Conductive Li6PS5Cl Argyrodite-Type Solid Electrolytes Using Pyridine Solvent. *ACS Appl. Energy Mater.* **2022**, *5*, 9266−9272.
(73) Kraft, M. A.; Culver, S. P.; Calderon, M.; Boöcher, F.; Krauskopf, T.; Senyshyn, A.; Dietrich, C.; Zevalkink, A.; Janek, J.; Zeier, W. G. Influence of lattice polarizability on the ionic conductivity in the lithium superionic argyrodites Li6PS5X (X = Cl, Br, I). *J. Am. Chem. Soc.* **2017**, *139*, 10909−10918.
(74) Hanghofer, I.; Brinek, M.; Eisbacher, S.; Bitschnau, B.; Volck, M.; Hennige, V.; Hanzu, I.; Rettenwander, D.; Wilkening, H. Substitutional disorder: structure and ion dynamics of the argyrodites Li 6 PS 5 Cl, Li 6 PS 5 Br and Li 6 PS 5 I. *Phys. Chem. Chem. Phys.* **2019**, *21*, 8489−8507.
(75) Morgan, B. J. Mechanistic origin of superionic lithium diffusion in anion-disordered Li6PS5 X argyrodites. *Chem. Mater.* **2021**, *33*, 2004−2018.
(76) Zhao, E.; He, L.; Zhang, Z.; Doux, J.-M.; Tan, D. H.; Wu, E. A.; Deysher, G.; Chen, Y.-T.; Zhao, J.; Wang, F.; Meng, Y. S. New insights into Li distribution in the superionic argyrodite Li 6 PS 5 Cl. *Chem. Commun.* **2021**, *57*, 10787−10790.
(77) Deng, Z.; Zhu, Z.; Chu, I.-H.; Ong, S. P. Data-driven first-principles methods for the study and design of alkali superionic conductors. *Chem. Mater.* **2017**, *29*, 281−288.
(78) Lee, B. D.; Lee, J.-W.; Park, J.; Cho, M. Y.; Park, W. B.; Sohn, K.-S. Argyrodite configuration determination for DFT and AIMD calculations using an integrated optimization strategy. *RSC Adv.* **2022**, *12*, 31156−31166.
(79) Jiang, M.; Chen, Z.-W.; Rao, A.; Chen, L.-X.; Zu, X.-T.; Singh, C. V. Se-doped Li6PS5Cl and Li 5.5 PS 4.5 Cl 1.5 with improved ionic conductivity and interfacial compatibility: a high-throughput DFT study. *J. Mater. Chem. C* **2022**, *10*, 18294−18302.
(80) Comer, J.; Gumbart, J. C.; Hénin, J.; Lelièvre, T.; Pohorille, A.; Chipot, C. The adaptive biasing force method: Everything you always wanted to know but were afraid to ask. *J. Phys. Chem. B* **2015**, *119*, 1129−1151.
(81) Pesko, D. M.; Webb, M. A.; Jung, Y.; Zheng, Q.; Miller, T. F., III; Coates, G. W.; Balsara, N. P. Universal relationship between conductivity and solvation-site connectivity in ether-based polymer electrolytes. *Macromolecules* **2016**, *49*, 5244−5255.
(82) Chu, W.; Webb, M. A.; Deng, C.; Colón, Y. J.; Kambe, Y.; Krishnan, S.; Nealey, P. F.; De Pablo, J. J. Understanding ion mobility in P2VP/NMP+ I-polymer electrolytes: a combined simulation and experimental study. *Macromolecules* **2020**, *53*, 2783−2792.
(83) Richter, D.; Kruteva, M. Polymer dynamics under confinement. *Soft Matter* **2019**, *15*, 7316−7349.
(84) Diddens, D.; Heuer, A. Simulation study of the lithium ion transport mechanism in ternary polymer electrolytes: the critical role of the segmental mobility. *J. Phys. Chem. B* **2014**, *118*, 1113−1125.
(85) Wang, Y.; Fan, F.; Agapov, A. L.; Saito, T.; Yang, J.; Yu, X.; Hong, K.; Mays, J.; Sokolov, A. P. Examination of the fundamental relation between ionic transport and segmental relaxation in polymer electrolytes. *Polymer* **2014**, *55*, 4067−4076.
(86) Zou, Z.; Li, Y.; Lu, Z.; Wang, D.; Cui, Y.; Guo, B.; Li, Y.; Liang, X.; Feng, J.; Li, H.; et al. Mobile ions in composite solids. *Chem. Rev.* **2020**, *120*, 4169−4221.
(87) Kühne, T. D.; Iannuzzi, M.; Del Ben, M.; Rybkin, V. V.; Seewald, P.; Stein, F.; Laino, T.; Khaliullin, R. Z.; Schütt, O.; Schiffmann, F.; et al. CP2K: An electronic structure and molecular dynamics software package-Quickstep: Efficient and accurate electronic structure calculations. *J. Chem. Phys.* **2020**, *152*, No. 194103.
(88) Jain, A.; Ong, S. P.; Hautier, G.; Chen, W.; Richards, W. D.; Dacek, S.; Cholia, S.; Gunter, D.; Skinner, D.; Ceder, G.; Persson, K. A. Commentary: The Materials Project: A materials genome approach to accelerating materials innovation. *APL Mater.* **2013**, *1*, No. 011002.
(89) Perdew, J. P.; Ruzsinszky, A.; Csonka, G. I.; Vydrov, O. A.; Scuseria, G. E.; Constantin, L. A.; Zhou, X.; Burke, K. Restoring the density-gradient expansion for exchange in solids and surfaces. *Phys. Rev. Lett.* **2008**, *100*, No. 136406.
(90) Goedecker, S.; Teter, M.; Hutter, J. Separable dual-space Gaussian pseudopotentials. *Phys. Rev. B* **1996**, *54*, No. 1703.
(91) Hartwigsen, C.; Gœdecker, S.; Hutter, J. Relativistic separable dual-space Gaussian pseudopotentials from H to Rn. *Phys. Rev. B* **1998**, *58*, No. 3641.
(92) Krack, M. Pseudopotentials for H to Kr optimized for gradient-corrected exchange-correlation functionals. *Theor. Chem. Acc.* **2005**, *114*, 145−152.
(93) VandeVondele, J.; Hutter, J. Gaussian basis sets for accurate calculations on molecular systems in gas and condensed phases. *J. Chem. Phys.* **2007**, *127*, No. 114105.
(94) Nosé, S. A unified formulation of the constant temperature molecular dynamics methods. *J. Chem. Phys.* **1984**, *81*, 511−519.
(95) Hoover, W. G. Canonical dynamics: Equilibrium phase-space distributions. *Phys. Rev. A* **1985**, *31*, No. 1695.
(96) Sun, W.; Ceder, G. Efficient creation and convergence of surface slabs. *Surf. Sci.* **2013**, *617*, 53−59.
(97) Ong, S. P.; Richards, W. D.; Jain, A.; Hautier, G.; Kocher, M.; Cholia, S.; Gunter, D.; Chevrier, V. L.; Persson, K. A.; Ceder, G. Python Materials Genomics (pymatgen): A robust, open-source python library for materials analysis. *Comput. Mater. Sci.* **2013**, *68*, 314−319.
(98) Storn, R.; Price, K. Differential evolution-a simple and efficient heuristic for global optimization over continuous spaces. *J. Global Optim.* **1997**, *11*, 341.
(99) Lampinen, J. In *A Constraint Handling Approach for the Differential Evolution Algorithm*. Proceedings of the 2002 Congress on Evolutionary Computation. CEC02 (Catal. No. 02TH8600), 2002; pp 1468−1473.
(100) Wormington, M.; Panaccione, C.; Matney, K. M.; Bowen, D. K. Characterization of structures from X-ray scattering data using genetic algorithms. *Philos. Trans. R. Soc., A* **1999**, *357*, 2827−2848.
(101) Thompson, A. P.; Aktulga, H. M.; Berger, R.; Bolintineanu, D. S.; Brown, W. M.; Crozier, P. S.; in 't Veld, P. J.; Kohlmeyer, A.; Moore, S. G.; Nguyen, T. D.; Shan, R.; Stevens, M. J.; Tranchida, J.; Trott, C.; Plimpton, S. J. LAMMPS - a flexible simulation tool for particle-based materials modeling at the atomic, meso, and continuum scales. *Comput. Phys. Commun.* **2022**, *271*, 108171.
(102) Molinari, N.; Khawaja, M.; Sutton, A.; Mostofi, A. Molecular model for hnbr with tunable cross-link density. *J. Phys. Chem. B* **2016**, *120*, 12700−12707.
(103) Watkins, E. K.; Jorgensen, W. L. Perfluoroalkanes: Conformational analysis and liquid-state properties from ab initio and Monte Carlo calculations. *J. Phys. Chem. A* **2001**, *105*, 4118−4125.
(104) Plimpton, S.; Pollock, R.; Stevens, M. Particle-Mesh Ewald and rRESPA for Parallel Molecular Dynamics Simulations. In *PPSC* 1997.

https://doi.org/10.1021/acsami.4c07440
ACS Appl. Mater. Interfaces XXXX, XXX, XXX−XXX